ACS APPLIED MATERIALS & INTERFACES

www.acsami.org

Research Article

# Correlating Antiagglomerant Performance with Gas Hydrate Cohesion

Anh Phan, Michail Stamatakis, Carolyn A. Koh, and Alberto Striolo*

Cite This: *ACS Appl. Mater. Interfaces* 2021, 13, 40002–40012

Read Online

ACCESS | Metrics & More | Article Recommendations | Supporting Information

**ABSTRACT:** Although inhibiting hydrate formation in hydrocarbon–water systems is paramount in preventing pipe blockage in hydrocarbon transport systems, the molecular mechanisms responsible for antiagglomerant (AA) performance are not completely understood. To better understand why macroscopic performance is affected by apparently small changes in the AA molecular structure, we perform molecular dynamics simulations. We quantify the cohesion energy between two gas hydrate nanoparticles dispersed in liquid hydrocarbons in the presence of different AAs, and we achieve excellent agreement against experimental data obtained at high pressure using the micromechanical force apparatus. This suggests that the proposed simulation approach could provide a screening method for predicting, *in silico*, the performance of new molecules designed to manage hydrates in flow assurance. Our results suggest that entropy and free energy of solvation of AAs, combined in some cases with the molecular orientation at hydrate–oil interfaces, are descriptors that could be used to predict performance, should the results presented here be reproduced for other systems as well. These insights could help speed up the design of new AAs and guide future experiments.

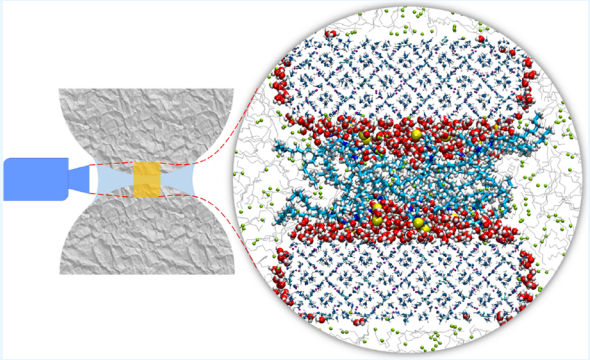

**KEYWORDS:** *molecular dynamics, configurational entropy, cohesive force, gas hydrate agglomeration, enthalpy of solvation, solvation free energy*



## INTRODUCTION

Gas hydrates are ice-like crystalline solids composed of polyhedral hydrogen-bonded water cages in which small gas molecules, *e.g.*, methane and carbon dioxide, are encapsulated. Gas hydrates are relevant for a variety of sectors, including energy, environment, and sustainability. With the goal of increasing the sustainability of our society, recent research advances have extended the utilization of gas hydrates in various applications, including but not limited to hydrogen and energy storage,[1−4] $CO_2$ capture and sequestration,[5−7] water desalination,[8,9] gas separation,[10,11] refrigeration and transport,[12] *etc.* Naturally occurring gas hydrates attract considerable attention for their potential role in providing an alternative energy source, although their environmental impacts should be mitigated.[12,13] On the other hand, safety in the energy sector is frequently associated with the prevention of hydrate agglomeration in oil/gas pipelines.[14] The formation, agglomeration, and deposition of gas hydrates can cause flowline blockages, affecting deep-water drilling, oil/gas transport, and processing facilities, potentially leading to severe environmental and economic impacts.[15−17]

In this context, flow assurance activities are experiencing a remarkable change from "hydrate avoidance" to "hydrate management", toward reducing capital and operational costs.[18−20] Hydrate inhibitors are commonly used to prevent the agglomeration of solid hydrate particles or their deposition on pipe walls. Depending on the expected inhibition mechanism, low-dosage hydrate inhibitors can be categorized as kinetic hydrate inhibitors (KHIs) and/or antiagglomerants (AAs).[14,15,21] KHIs and AAs can be effective at dosages in the range of 0.5−2 vol %, while thermodynamic hydrate inhibitors require dosages of as high as 30−40 vol %.[21−23] However, the AA performance and their minimum effective dosage in specific applications vary, thereby affecting significantly the production costs. Although numerous studies have focused on understanding hydrate–hydrocarbon/water systems in the presence of AAs,[24−33] many experimental[28,29,34] and computational[30−32] efforts are made under conditions somewhat far from those relevant in practice.

Insights into AA mechanisms of action have been obtained by measuring cohesive and adhesive forces.[35,36] After overcoming initial difficulties, the micromechanical force (MMF) apparatus has shown great practical and fundamental potential

Received: April 6, 2021
Accepted: July 20, 2021
Published: August 12, 2021

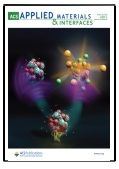

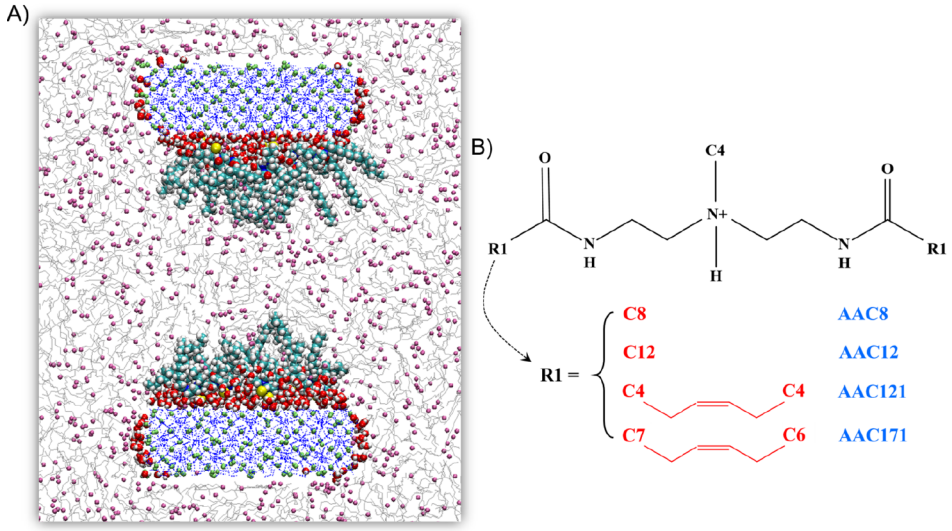


**Figure 1.** (A) Representative simulation snapshot for the final configuration for a system composed of two sII hydrate particles covered with thin water films and AAs, immersed in a mixture of gaseous ($CH_4$—$C_2H_6$) and liquid hydrocarbons. Blue dotted lines symbolize water molecules in the hydrate. Purple and green spheres symbolize methane/ethane in the liquid and hydrate phases, respectively. Silver lines represent liquid hydrocarbons, *e.g.*, *n*-dodecane and *n*-heptane. Red and white spheres represent water oxygen and hydrogen atoms, respectively. Cyan, blue, red, white, and yellow spheres represent carbon, nitrogen, oxygen, hydrogen atoms in AA molecules, and chloride ions, respectively. (B) Molecular structures of the AAs considered: AAC8 (R1 = C8), AAC12 (R1 = C12), AAC121 (R1 = C4—C—C═C—C—C4), and AAC171 (R1 = C7—C—C═C—C—C6).

because it measures directly hydrate interparticle cohesive forces.[23,37,38] For example, Dieker et al.[39] and Aman et al.[40] investigated the effect of carboxylic acids and crude oils on cyclopentane (CyC5) hydrate particle interactions. Assuming that capillary cohesion governs hydrate interparticle forces, the results suggest that surfactants could disturb the liquid bridge formed between hydrate particles, potentially reducing the cohesive forces.[39,40] Most previous studies were conducted using hydrates that are stable at atmospheric pressure, for example, using hydrates of tetrahydrofuran (THF)[41] and CyC5,[23,28,37,38,42,43] although the conditions are different compared to those realistically experienced in typical flow assurance applications (high pressures and low temperatures). To probe realistic conditions, the high-pressure micromechanical force (HP-MMF)[44] apparatus was designed to quantify cohesive forces between ice particles and natural gas hydrate particles in both gas[44,45] and liquid hydrocarbons.[46−48] Recently, Koh and coworkers[48] employed the HP-MMF apparatus to measure $CH_4/C_2H_6$ hydrate cohesive forces in the presence of AAs. The flow assurance performance of those AAs was assessed using a rocking cell apparatus, as frequently done in industry. Comparing the data sets obtained, it was found that those AAs that substantially decrease the cohesive forces can show good overall performance in the rocking cell.[48] Of note, the molecular structure of the AAs used in these experiments was known, and in fact, it had been used in prior atomistic molecular dynamics (MD) simulations by Striolo and his collaborators.[31,33,49,50] These simulations suggested that AAs that yield an ordered structure at the hydrate−oil interface can exhibit good practical performance. If MD simulations were consistent with HP-MMF experiments, then a seamless workflow could correlate AA molecular structures, their self-assembly at the hydrate−oil interface, their effect on hydrate−hydrate cohesive forces, and their macroscopic flow assurance performance, thereby providing a tool for the *in silico* design and screening of new potential AA molecules. The goal of this manuscript is to test whether such correlations are possible. While new MD simulation results are presented in this article, the experimental data are taken from the study by Koh et al.[48]

## SIMULATION METHODOLOGY

**Model Setup.** One representative simulation setup (see Figure 1A) mimics the measurements of hydrate particle cohesive forces conducted in experiments.[48] Each simulated system contains two hydrate nanoparticles immersed in a hydrocarbon mixture. Each hydrate nanoparticle was carved out of the bulk structure of sII $CH_4/C_2H_6$ hydrates.[51] These hydrates were used in the HP-MMF apparatus and are expected to form within rocking cell experiments[48] to test the AA performance . The *X*, *Y*, and *Z* dimensions of each hydrate nanoparticle were 5.193, 3.462, and 1.731 nm, respectively. The hydrate substrates were parallel to the *X*−*Y* plane. On top of the hydrate particles, we deposited a thin water film with a thickness of ∼0.5 nm and a layer of quaternary ammonium surfactant AAs along the *Z* direction.[31,42,49,50] Thereafter, we duplicated the hydrate nanoparticle covered with water and AAs and placed the two hydrate nanoparticles in a mirror-symmetric way along the *Z* direction. The two hydrate nanoparticles were then immersed in the hydrocarbon phase, yielding simulation box lengths of 11.193, 3.462, and 16 nm in the *X*, *Y* and *Z* directions, respectively. The hydrate substrates are infinite along the *Y* direction due to the periodic boundary conditions applied in three directions.

In our simulations, the hydrocarbon phase contains either *n*-dodecane or *n*-heptane and $CH_4/C_2H_6$ gas mixtures with a molar ratio of 10:7.5:2.5. The gas mixture used in this study consists of 75 mol % of methane and 25 mol % of ethane, similar to the Green Canyon gases used in experiments.[48] The AAs considered are AAC8, AAC12, AAC121, and AAC171 (their structures are shown in Figure 1B) at an AA surface density of 0.44 molecule/nm$^2$. The AAC171 was also


https://doi.org/10.1021/acsami.1c06309
ACS Appl. Mater. Interfaces 2021, 13, 40002−40012

**Table 1. Compositions of the Simulated Systems**

| | $N_{CH_4\text{-sII}}$ | $N_{C_2H_6\text{-sII}}$ | $N_{H_2O\text{-sII}}$ | $N_{H_2O}$ | $N_{AAs}$ | $N_{C12}$: $N_{CH_4}$: $N_{C_2H_6}$ | $N_{C7}$: $N_{CH_4}$: $N_{C_2H_6}$ |
|---|---|---|---|---|---|---|---|
| AAs-0.44 | 216 | 72 | 1632 | 600 | 16 | 1160:870:290 | 1800:1350:450 |
| AAC171-0.28 | 216 | 72 | 1632 | 600 | 10 | 1160:870:290 | 1800:1350:450 |

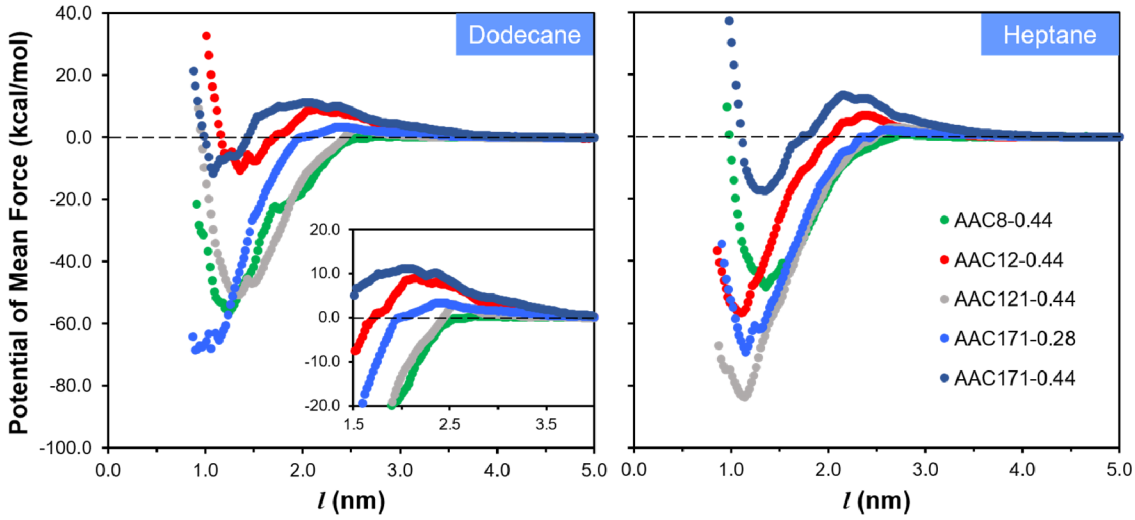


**Figure 2.** PMF profiles along the $Z$ direction (perpendicular to the hydrate surfaces) as experienced by one hydrate particle moving toward the other in the presence of *n*-dodecane (left) and *n*-heptane (right). The results were obtained for the hydrate particles covered with AAC8 (green), AAC12 (red), AAC121 (gray), and AAC171 (dark blue) at a surface density of 0.44 molecule/nm$^2$ and AAC171 at a surface density of 0.28 molecule/nm$^2$ (bright blue). The distance $l$ is that between the planes formed by the water oxygen atoms of the surfaces of bottom and top hydrate nanoparticles, which are in contact with thin water films and AAs.

simulated at a surface density of 0.28 molecule/nm$^2$, which, in our approximation (based on the ratio of the reciprocals of two quantities, *e.g.*, the number of AA molecules and the molecular weight of AAs), should correspond to similar bulk AA concentration (in liquid hydrocarbons) as those for systems with AAC8, AAC12, and AAC121 at a surface density of 0.44 molecule/nm$^2$. It should be noted that experimental data are not available for the AAC121 surfactant, which was considered here, for illustration purposes, as a potential new AA, designed *in silico*. In Table 1, we report the compositions of the simulated systems.

**Force Fields and Implementation.** Water molecules were represented by the TIP4P/Ice model,[52] which has been proven to be successful in simulating hydrate nucleation and growth[5,53] as well as studying the effectiveness of potential hydrate AAs.[31,49] AAs were modeled using the general Amber force field,[54,55] often employed to study organic and pharmaceutical molecules containing H, C, N, O, S, P, and halogens.[54] Hydrocarbons (*e.g.*, methane, ethane, *n*-dodecane, and *n*-heptane) were described by implementing the united atom version of the TraPPE-UA force field,[56] which accurately characterizes the vapor−liquid coexistence curves and critical properties of linear alkanes from methane to dodecane. We added chloride ions ($Cl^-$) represented as charged Lennard-Jones spheres[57] to maintain system charge neutrality. The chloride ions ($Cl^-$) were modeled using the potential parameters taken from the study by Dang without polarizability[57] because this force field is compatible with various water models.[58,59] All nonbonded interactions were characterized by dispersion and electrostatic forces using the 12-6 Lennard-Jones (LJ) and Coulombic potentials, respectively. We employed the particle−particle particle−mesh (PPPM) method for treating long-range corrections[60] and the Lorentz−Berthelot mixing rules to characterize the unlike LJ interactions.[61] A cutoff distance of 14 Å was used for all interactions.

Equilibrium MD simulations were conducted using the GROMACS package,[62] version 2016.3. We implemented simulation procedures similar to those used in our previous study.[31,49] First, we performed an NVT canonical ensemble simulation for 1 ns to relax the initial configuration, while the hydrate layer was kept fixed. Subsequently, the simulations were carried out within the NPT ensemble under conditions similar to the experiments ($T$ = 274 K and $P$ = 3.45 MPa) using a Nose−Hoover thermostat and Berendsen/Parrinello−Rahman barostat.[62] We implemented the pressure coupling only along the $Z$ direction, which enables us to keep $X$ and $Y$ dimensions of the simulation box constant. The equations of motion were solved using the leapfrog algorithm with a time step of 1.0 fs.[62] We applied a harmonic restraint force ($k$ = 2000 kJ/mol nm) on water, methane, and ethane molecules in the two hydrate nanoparticles to tether them to their initial positions,[62] while other molecules in the system were allowed to move in the NPT simulations. We conducted each NPT simulation for ≥200 ns. To check whether the simulations reach equilibrium, we analyzed the convergence of system density and energy as well as density profiles of *n*-dodecane (or *n*-heptane) along the direction of the simulation box perpendicular to the hydrate particles.

Once equilibration was reached, we conducted umbrella sampling (US) simulations[62] to examine the interaction forces between the two hydrate nanoparticles in the presence of various AAs, which have been investigated experimentally. The results from the US simulations were reconstructed to calculate the potential of mean force (PMF) experienced by one hydrate nanoparticle moving toward the other along the $Z$ direction.


https://doi.org/10.1021/acsami.1c06309
ACS Appl. Mater. Interfaces 2021, 13, 40002−40012

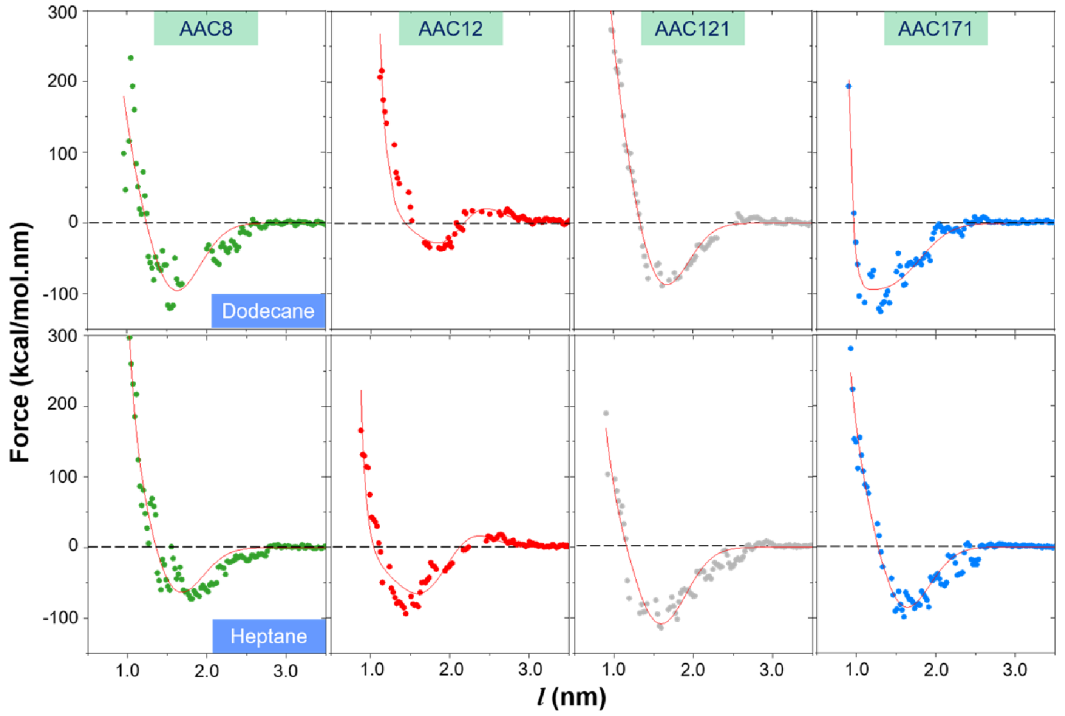


**Figure 3.** Simulated force−distance curves obtained for the hydrate particles in *n*-dodecane (top) and *n*-heptane (bottom). Red lines represent the fitting of data points to a mathematical function (eq 1). The results were obtained for the hydrate particles covered with AAC8 (green), AAC12 (red), and AAC121 (gray) at the surface density of 0.44 molecule/nm$^2$ and AAC171 at the surface density of 0.28 molecule/nm$^2$ (bright blue).

The center of mass of the pulling hydrate particle was tethered by a harmonic spring of elastic constant 2000 kJ/mol nm. During the US simulations, water, methane, and ethane molecules in the pulling hydrate particle were allowed to move freely, while water−methane and water−ethane distances were constrained within the hydrate particles to maintain the sII hydrate structure. In each sampling window, a US run of 20 ns was conducted in the NVT ensemble. The weighted histogram analysis method algorithm was used to reconstruct the PMF profiles.[63] The bootstrap analysis employed in GROMACS was conducted to estimate the error bars.[63]

## RESULTS AND DISCUSSION

**Potential of Mean Force.** In Figure 2, we present the PMF profiles experienced by the two hydrate particles as they approach each other in the direction perpendicular to the hydrate−hydrocarbon interface. The results are shown for two liquid hydrocarbons: *n*-dodecane (left) and *n*-heptane (right). The PMF profiles were obtained as a function of the distance $l$ between the surfaces of the two hydrates (see Figure 1A). The results depend strongly on the AAs used. Specifically, in the presence of AAC8 (green), the PMF profile shows an effective attraction between the two hydrate particles. On the other hand, the PMFs obtained in the presence of AAC12 (red), AAC121 (gray), and AAC171 (at both surface densities considered—dark and bright blue, respectively) show, as the distance decreases, one repulsive barrier at intermediate $l$, a subsequent minimum, and a monotonic increase as $l$ decreases. The repulsive barrier represents the work needed to compress and disperse the AA layers, which is dependent on the structural conformations of the AAs, *e.g.*, tail length, tail configurations (e.g., inclusion of double bonds), packing density (AA surface densities at 0.44 and 0.28 molecule/nm$^2$), and the properties of solvents.[64] Much higher repulsive barriers are obtained in the presence of AAC12 (red) and AAC171 (dark blue), at a surface density of 0.44 molecule/nm$^2$, in both *n*-dodecane and *n*-heptane. Analysis of the density profiles for the AA films confined between the two hydrate particles when they are at a relative distance of $l$ = 2.51 nm, where the PMF shows a repulsive barrier for the system with AAC12, indicates a more pronounced density peak for the system with AAC12 compared to the results obtained for the systems with AAC8 and AAC121 (as shown in Figure S1). One significant feature in the PMFs seems to strongly depend on the liquid hydrocarbon; specifically, the hydrates covered with AAC12 in *n*-heptane experience stronger attraction than those in *n*-dodecane when they begin to interact, whereas the interactions between the hydrates covered with AAC8 in *n*-dodecane are more attractive than those in *n*-heptane.

Varying AAs and the liquid hydrocarbon alters significantly the maximum distance at which the two hydrates experience an effective attraction (the PMF decreases below 0) (see Table S1). Specifically, the effective attraction between two hydrate particles covered with AAs in both *n*-dodecane and *n*-heptane is observed at a distance $l$, which increases in the following order: AAC171-0.44 < AAC12-0.44 < AAC171-0.28 < AAC121-0.44 < AAC8-0.44. The hydrate particles covered with AAC12, AAC121, and AAC171 in *n*-heptane seem to attract each other at distances further than when they are in *n*-dodecane. These results offer qualitative understanding of the dispersion behavior of hydrate particles under the effect of various AAs and liquid HCs and provide some insights into the AA performance.

**Force−Distance Profiles.** By differentiation of the PMF profiles, we can obtain effective force−distance curves by $\langle F(l)\rangle = -\mathrm{dPMF}(l)/dl$. The differentiation is conducted numerically by implementing a backward difference approximation. The resultant force−distance profiles are reminiscent


https://doi.org/10.1021/acsami.1c06309
ACS Appl. Mater. Interfaces 2021, 13, 40002−40012

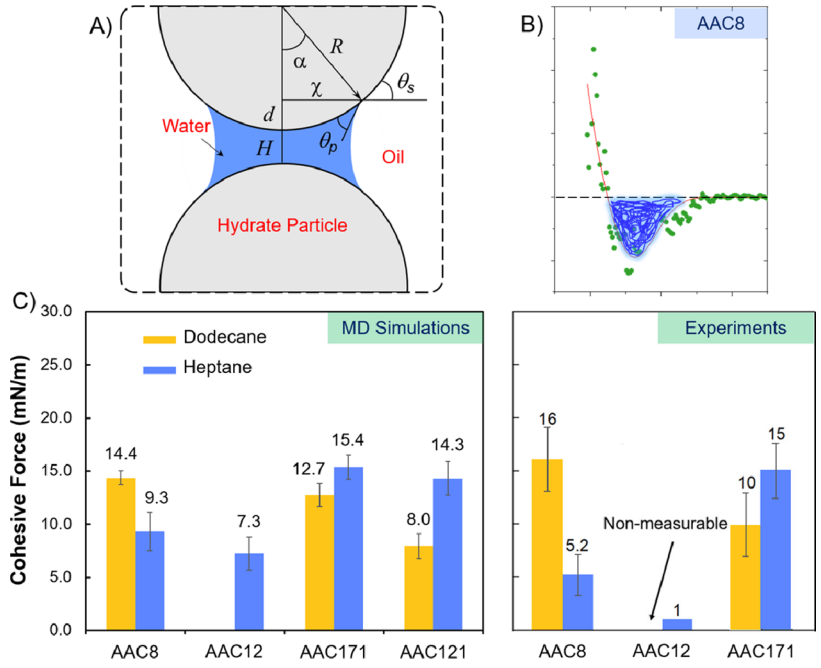


**Figure 4.** (A) Schematic of particle−particle capillary cohesion with the following parameters: particle radius ($R$), particle separation distance ($H$), liquid bridge immersion depth ($d$), capillary bridge width ($\chi$), embracing angle ($\alpha$), external contact angle ($\theta_s$), and contact angle ($\theta_p$), adapted with permission from ref 37 Copyright 2012 Elsevier B.V. (B) Schematic of the calculation for cohesive work attributed to hydrate−hydrate cohesion (blue shaded region under the line of zero value of force). (C) Experimental and simulated cohesive force data between two hydrate particles covered with AAs immersed in *n*-dodecane (yellow) and *n*-heptane (blue). Simulation results were obtained in the presence of AAC8, AAC12, and AAC121 at a surface density of 0.44 molecule/nm$^2$ and AAC171 at a surface density of 0.28 molecule/nm$^2$. The results obtained from MD simulations (left, this work) and HP-MMF experiments (right, adapted with permission from ref 48 Copyright 2021 American Chemical Society) are shown. In the experimental data, the surface density of AAs is not known, although all experiments were conducted at an AA concentration of 0.5 vol %. Pressure and temperature conditions considered in the experiments are the same as those used in the simulations: 3.45 MPa and 274 K.

of a Lennard-Jones force (with parameters $\varepsilon$ and $\sigma$, which illustrate the depth of the attractive well and the distance at which the interaction potential is zero, respectively) superimposed to a repulsive force between the hydrate particles (with parameters $r_o$, $b$, and $n$, which control the position and height of the repulsive peak), yielding the following expression:[65]

$$F = 4\varepsilon\left(\frac{12\sigma^{12}}{r^{13}} - \frac{6\sigma^{6}}{r^{7}}\right) \times \left(1 - \sqrt{\pi}\,\exp\left[\frac{-(r - r_o)^2}{b}\right] \times n\right) \quad (1)$$

Fitting simulated force data points to eq 1 via adjusting the parameters $\varepsilon$, $\sigma$, $r_o$, $b$, and $n$ (the values are reported in the Supporting Information) employing a nonlinear regression with the Levenberg−Marquardt algorithm and removing outliers following the protocol suggested by Motulsky and Brown (the details of the numerical procedure are given in the Supporting Information),[66] we observe that the force−distance profiles for the systems with AAC12 in the presence of *n*-dodecane and *n*-heptane (see Figure 3, top and bottom, respectively) present mid-range moderately repulsive peaks. These repulsions could prevent coalescence if strong enough, which is the aim of using AAs for hydrate management. The results present a different situation for the systems with AAC8 (green), AAC121 (gray), and AAC171 at AA surface density of 0.28 molecule/nm$^2$ (bright blue) in *n*-dodecane (Figure 3, top) and *n*-heptane (Figure 3, bottom). For these systems, the force profiles are consistent with an effective attraction between the two hydrates, even in the presence of the AAs. These simulation results suggest that AAC12 might exhibit good antiagglomerant performance in *n*-dodecane and *n*-heptane compared to the other AAs at the same vol % in the hydrocarbon phase. These expectations are indeed qualitatively consistent with experimental observations.[48]

**Hydrate Particle Cohesive Forces.** To quantitatively compare the simulation results with the experimental data reported by Koh et al.,[48] we quantify the cohesive force. The hydrate interparticle cohesive force measurements are interpreted using the capillary bridge theory[36,67−69]

$$\frac{F_A}{R^*} = 2\pi\gamma\,\sin(\alpha)\,\sin(\theta_p + \theta_s) + \frac{2\pi\gamma\,\cos\theta_p}{1 + \frac{H}{2d}} \quad (2)$$

In eq 2, $F_A$ is the hydrate interparticle cohesive force, $R^*$ is the harmonic mean radius of the particle pair, and other relevant parameters are described in Figure 4A.

Assuming that the pressure difference between the bulk phases and the bridge (capillary pressure) is extremely small for the systems considered in the current investigation, the cohesive force between two nanoparticles can be described by the following expression, where the first term of eq 2 is modified to take into account only the particle−particle contact area and the second term of eq 2 is removed:[37]

$$\frac{F}{L^*} = \frac{W_{sep}}{A} \quad (3)$$


https://doi.org/10.1021/acsami.1c06309
ACS Appl. Mater. Interfaces 2021, 13, 40002−40012

In eq 3, $F$ is the hydrate−hydrate cohesive force, $W_{sep}$ is the work of separation of two hydrate nanoparticles or also the hydrate−hydrate work of cohesion (illustrated as the blue shaded region in Figure 4B), $L^*$ is the harmonic mean circumference of the hydrate particle pair, and $A$ is the surface area of the interface.

In Table 2, we report the work of cohesion $W_{sep}$ for the systems with AAC8, AAC12, and AAC121 at an AA surface density of 0.44 molecule/nm$^2$ and AAC171 at an AA surface density of 0.28 molecule/nm$^2$ in the presence of *n*-dodecane and *n*-heptane. $W_{sep}$ is determined by the integration of the force−distance curves under the reference line at $F = 0$ until the force approaches the zero value.[70] The results show negative $W_{sep}$ only for the case in which the two hydrate nanoparticles covered with AAC12 in *n*-dodecane are brought closer together. This suggests that the cohesive force measurement for this system is inaccessible, which is in excellent agreement with recent experimental data.[48] On the other hand, we observe positive values of $W_{sep}$ for all of the other systems.

**Table 2. Work of Cohesion for the Systems with AAC8, AAC12, and AAC121 at the AA Surface Density of 0.44 molecule/nm$^2$ and AAC171 at the AA Surface Density of 0.28 molecule/nm$^2$ in the Presence of *n*-Dodecane and *n*-Heptane**

| | work of cohesion (kcal/mol) | |
|---|---|---|
| | *n*-dodecane | *n*-heptane |
| AAC8-0.44 | 74.35 ± 3.40 | 48.23 ± 9.44 |
| AAC12-0.44 | −2.58 ± −0.70 | 37.54 ± 8.08 |
| AAC121-0.44 | 41.14 ± 6.06 | 74.15 ± 8.18 |
| AAC171-0.28 | 65.94 ± 5.57 | 79.61 ± 5.88 |

When values for the work of cohesion are known, we further quantify the cohesive force ($F/L^*$) in eq 4. In Figure 4C, left, we show the cohesive force calculated for the systems with AAC8, AAC12, and AAC121 at a surface density of 0.44 molecule/nm$^2$ and AAC171 at a surface density of 0.28 molecule/nm$^2$ in *n*-dodecane and *n*-heptane. The cohesive force found in the presence of AAC8 in *n*-dodecane is larger than that obtained in *n*-heptane, suggesting that AAC8 performs better as an AA in the latter than in the former hydrocarbon, whereas the results obtained for AAC12, AAC121, and AAC171 show opposite trends. Our previous MD study also suggested that AAC12 might perform better in *n*-dodecane than in *n*-octane and in *n*-hexane.[31] Because our simulation results are quantitatively comparable to experimental measurements (see Figure 4C, right),[48] we propose that the simulation protocol implemented here could be used to predict AA performance. For example, the AAC121 surfactant was not considered in the experimental procedure reported by Koh et al.[48] The MD results presented in Figure 4C suggest that this molecule might not be a good AA candidate in either liquid hydrocarbon for use in flow assurance, as it yields measurable and rather high cohesive forces between the hydrates.

**AA Orientation.** In an attempt to identify molecular features that correlate with the cohesive force data shown in Figure 4C, we examine the orientation of AAs adsorbed on the hydrate surfaces. Previous studies suggested that the orientational ordering of AAs could help predict AA performance in

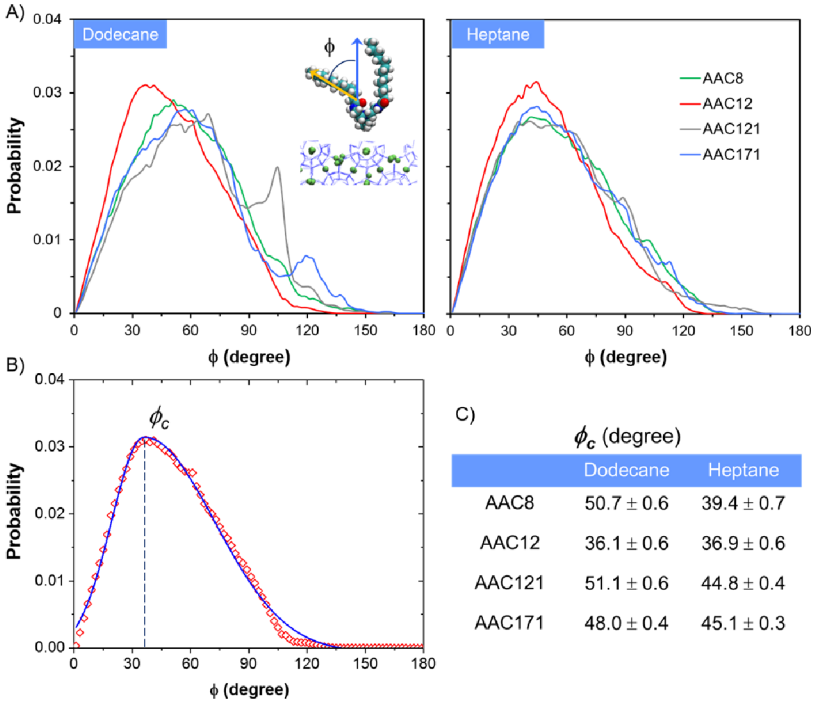


**Figure 5.** (A) Probability distributions of the orientational angle $\phi$ for AAC8 (green), AAC12 (red), and AAC121 (gray) at 0.44 molecule/nm$^2$ and AAC171 at 0.28 molecule/nm$^2$ (bright blue). The results were obtained in *n*-dodecane (left) and *n*-heptane (right). The inset in the left panel shows a diagram describing the orientational angle $\phi$ formed by the vector connecting the first to the last carbon atom of the AA long tails and the direction perpendicular to the hydrate surface. (B) Fitting data points of the probability distribution of the orientational angle with a skew Gaussian curve. (C) Global maximum of the Gaussian hills $\phi_c$ obtained from fitting the probability distribution of the orientational angle for all systems considered.


https://doi.org/10.1021/acsami.1c06309
ACS Appl. Mater. Interfaces 2021, 13, 40002−40012

hydrate management (the more uprightly the AAs orient, the better they perform),[31,71] as a well-ordered AA film can effectively exclude $CH_4/C_2H_6$ from the interfacial layer, which possibly hinders hydrate growth.[31,50] To quantify the AA orientation, we calculate the probability distribution of the orientational angle $\phi$ formed between each surfactant tail and the surface normal, *e.g.*, *Z* direction. For all AAs, we observe wide probability distributions at the low AA surface densities considered here (see Figure 5A), consistent with previous results.[31,33] These results suggest that the AAs remain orientationally disordered under the conditions probed in the present study. On fitting the probability distributions with skew Gaussian curves (see Figure 5B), we obtained the global maximum of the Gaussian hills $\phi_c$ for all systems considered (see Figure 5C). The $\phi_c$ value for AAC8 in *n*-heptane (39°) is smaller than that in *n*-dodecane (51°), which means that AAC8 molecules orient their long hydrocarbon tails more vertically in *n*-heptane than in *n*-dodecane, possibly explaining why AAC8 yields larger cohesive force in *n*-dodecane than in *n*-heptane. Nevertheless, the $\phi_c$ values for other AAs considered here do not correlate with the corresponding cohesive forces. For example, the $\phi_c$ values for AAC12 in both liquid hydrocarbons are rather comparable (36°−37°) despite the fact that AAC12 shows much better performance in *n*-dodecane. This suggests that, although the interfacial orientation might be important for explaining the AA performance at high AA surface densities, it might not be sufficient to explain cohesive energy data. Other mechanisms likely affect AA performance.

**Free-Energy and Entropy Changes on Solvation of AAs.** To determine which other molecular factors might affect the effectiveness of AAs in hydrate management, we recall the suggestion that hydrocarbons provide more favorable solvation free energy to longer hydrophobic AA tails.[26] Using the perturbation method coupled with the Bennett acceptance ratio protocol,[62] we analyzed the free-energy changes upon solvation of the AAC8, AAC12, and AAC12 at 0.44 molecule/nm$^2$ and AAC171 at 0.28 molecule/nm$^2$ in both *n*-dodecane (yellow) and *n*-heptane (blue), as shown in Figure 6A, filled circles. The results show that the AA solvation free energies computed in both liquid hydrocarbons are similar, although the corresponding cohesive forces are rather different (columns shown in Figure 6A). The solvation free energy of AAC12 is also comparable to that of AAC121 in *n*-dodecane and *n*-heptane, possibly because these surfactants have the same tail length, despite the fact that AAC12 shows much better performance than AAC121. Therefore, we conclude that the solvation free energy alone cannot explain the correlation between simulated and experimental data presented here, regarding AA flow assurance performance.

Because of the significant contribution of the entropy coupled with the conformational degrees of freedom to the thermodynamics of solvation of molecules,[72,73] we computed the configurational entropy, $S_L$, of AAs in liquid hydrocarbons via the method developed by Schlitter and others.[74−77] Note that the configurational entropy corresponds to the entropy associated with the intramolecular vibrations of a molecule,[78] and thus, analysis of configurational entropy of a molecule will provide insights into the degree of its flexibility.[79,80] $S_L$ is quantified by calculating the covariance of the Cartesian coordinates of atoms of one AA molecule with the following expression:[72]

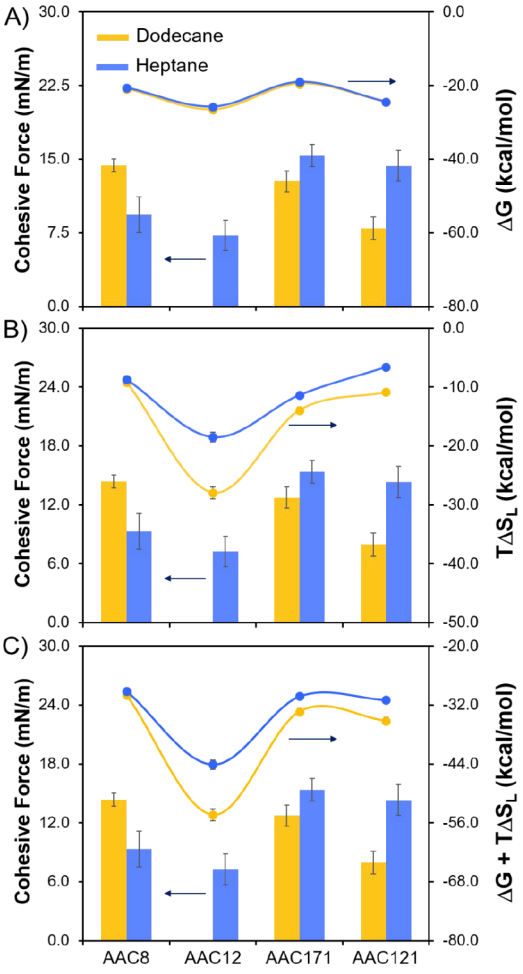


**Figure 6.** Simulated cohesive force (bars) between two hydrate particles covered with AAs immersed in *n*-dodecane (yellow) and *n*-heptane (blue) with free energy (A), entropy change (B), and sum of free energy and entropy change (C) associated with solvation of AA molecules in the presence of *n*-dodecane and *n*-heptane (yellow and blue, filled circles, respectively) at 274 K and 3.45 MPa. The computational results were obtained for the systems with AAC8, AAC12, AAC121, and AAC171.

$$S_L = \frac{1}{2}k \ln \det\left[1 + \frac{kTe^2}{\hbar}M^{1/2}\sigma M^{1/2}\right] \quad (4)$$

In eq 4, $M$ is the 3*N*-dimensional diagonal mass matrix for one AA of $N$ atoms, $\sigma$ is the covariance in positions of the AA atoms, $e$ is the Euler number, $T$ is the simulation temperature, and $k$ is the Boltzmann constant. The entropy change because of the reorganization of AAs in the presence of solvent at density $\rho$ can be estimated as $\Delta S_L = S_L(\rho) - S_L(\rho = 0)$.

We report the entropy change $T\Delta S_L$ (as shown in Figure 6B, filled circles) associated with solvation of AAC8, AAC12, and AAC12 at 0.44 molecule/nm$^2$ and AAC171 at 0.28 molecule/nm$^2$ in *n*-dodecane (yellow) and *n*-heptane (blue) at 274 K and 3.45 MPa. Note that the larger the entropy change upon solvation is, the more inflexible the AAs become when dissolved in the hydrocarbons, perhaps suggesting a higher efficiency in preventing $CH_4/C_2H_6$ from entering the interfacial layer. The results show that $T\Delta S_L$ values for AAC12, AAC171, and AAC121 in *n*-dodecane are larger than the corresponding values in *n*-heptane, suggesting that the AAs considered here are less flexible in *n*-dodecane than in *n*-


https://doi.org/10.1021/acsami.1c06309
ACS Appl. Mater. Interfaces 2021, 13, 40002−40012

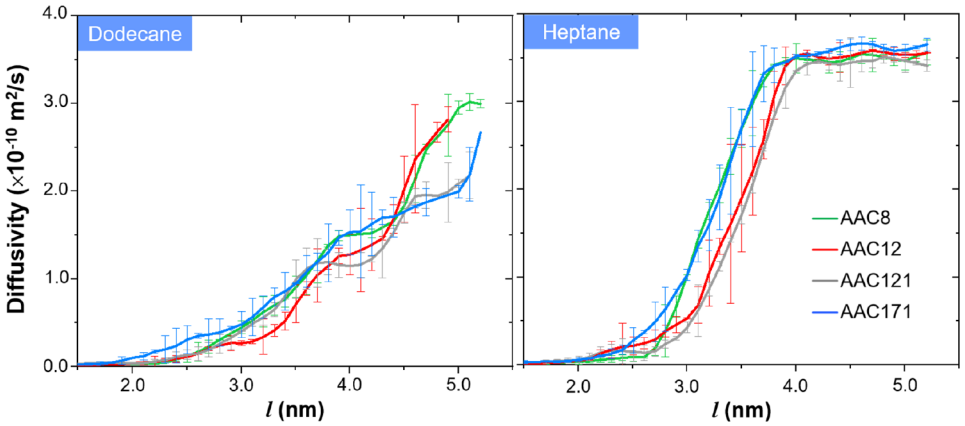


**Figure 7.** Diffusion profiles along the $Z$ direction for one hydrate particle moving toward the other in the presence of *n*-dodecane (left) and *n*-heptane (right). The results were obtained for the systems in the presence of AAC8 (green), AAC12 (red), and AAC121 (gray) at the AA surface density of 0.44 molecule/nm$^2$ and AAC171 at the AA surface density of 0.28 molecule/nm$^2$ (bright blue). Each line represents the diffusion profile for a hydrate particle with AAs, obtained by smoothing the diffusivity data using an adjacent averaging filter.

heptane, which possibly explains why the cohesive forces between two hydrate particles measured are smaller in *n*-dodecane. Contrarily, while $T\Delta S_L$ values for AAC171 in both liquid hydrocarbons are larger than the results obtained for AAC121, the cohesive forces between two hydrate particles covered with AAC171 are greater. In addition, $T\Delta S_L$ for AAC171 in *n*-heptane is higher than that calculated for AAC8, albeit the cohesive forces between two hydrate particles covered with AAC171 in *n*-heptane are larger. Thus, our results suggest no correlation between the entropy change upon solvation of AAs and their flow assurance performance, at least within our data set.

However, on combining free-energy and entropy changes associated with solvation of AAs, which represents the enthalpy of solvation ($\Delta G + T\Delta S_L$), we observe a direct correlation with AA performance, i.e., $\Delta G + T\Delta S_L$ data for AAs in *n*-dodecane follow the order: AAC12 > AAC121 > AAC171 > AAC8, which is consistent with the order obtained for the cohesive forces (see Figure 6C). To support our results, we note that Lynden-Bell et al.[81] previously identified a correlation between the solvation free energy of a nonpolar molecule and its hydration structure. We note that $\Delta G + T\Delta S_L$ for AAC8 in *n*-heptane is comparable to values calculated for AAC171 and AAC121 (∼−30.1±0.6 kcal/mol), although AAC8, AAC171, and AAC121 in *n*-heptane show significant differences in orientation (see Figure 5C). Similarly, $\Delta G + T\Delta S_L$ values for AAC8 in the two hydrocarbons considered here are equivalent, while the respective molecular orientation is different. This suggests that, when $\Delta G + T\Delta S_L$ values predicted for two AAs are similar, the AA orientation at the hydrate−hydrocarbon interface might correlate with macroscopic performance. Comparing the results obtained for AAC171 and AAC121, we conclude that including one double bond in the tails of these AAs increases their degree of flexibility and thereby reduces their effectiveness in preventing hydrate agglomeration. These observations suggest that the quantification of $\Delta G + T\Delta S_L$ changes on solvation of AA coupled with the AA orientation at the hydrate−oil interface, as well as cohesion force between hydrate particles could be used to predict AA performance. Certainly, more extensive data sets should be used to test whether this correlation has predictive capabilities.

One might wonder why AAC12 molecules orient their *n*-dodecyl tails more uprightly and become less flexible in *n*-dodecane than in *n*-heptane compared to the other AAs (see Figure 5). Employing neutron and X-ray diffraction techniques, Clarke and his coworkers[82] found that dodecane forms additional phases with parallel and upright molecular structures, even at high temperature (290 K), at both low and high coverages, in contrast to other hydrocarbons. This could help us understand previous observations according to which mixtures of surfactants with *n*-dodecyl tails with dodecane could yield ordered interfacial monolayers, while ordered interfacial films could not be observed for mixed *n*-octyl-octane[31] or *n*-hexyl-hexane[83] monolayers.

**Dynamic Properties.** To complement the thermodynamic analysis, we estimated the position-dependent diffusion profiles, thereby obtaining molecular-level understanding of the transport of hydrate particles covered with AAs across the hydrocarbon phase. The variation of the hydrate particle diffusivity can be affected by the variation of the frictional environment as the particle moves from the bulk hydrocarbon phase toward the other particle. Due to the heterogeneity of simulated systems, the calculation of the position-dependent diffusion constant is more reliable than the quantification of mean square displacements.[84] It is worth noting that the ability to suspend/disperse hydrate particles in a liquid hydrocarbon phase is important for hydrate slurry transport. We extended the standard scope of the US framework considering the method introduced by Straub and coworkers[85] and elaborated by Hummer,[86] where the position-dependent diffusion coefficient is computed from the position autocorrelation function (PACF) obtained from harmonically restrained simulations:[32,71,87]

$$D(z_k = \langle z \rangle_k) = \frac{\mathrm{var}(z)^2}{\int_0^\infty C_{zz}(t)\,\mathrm{d}t} \tag{5}$$

In eq 5, $\langle z \rangle_k$ is the average of the Cartesian position of the hydrate particle along the $Z$ direction in the US window $k$, $C_{zz}(t) = \langle \delta z(0) \delta z(t) \rangle$ is the PACF calculated directly from the time series, and $\mathrm{var}(z) = \langle z^2 \rangle - \langle z \rangle^2$ is its variance.

Our results, in Figure 7, show that the hydrocarbon phase strongly affects the diffusion profiles of the hydrate particles. In particular, the hydrate particles diffuse in bulk *n*-heptane (∼3.5 × 10$^{-10}$ m$^2$/s) faster than in *n*-dodecane (∼3.0 × 10$^{-10}$ m$^2$/s), probably due to the lower viscosity of *n*-heptane. Varying AAs


https://doi.org/10.1021/acsami.1c06309
ACS Appl. Mater. Interfaces 2021, 13, 40002−40012

moderately alters the diffusion of the hydrate particles. Specifically, the diffusivities of the hydrate particles covered with AAC12 and AAC121 in *n*-heptane are slower than those covered with AAC8 and AAC171 when the two hydrate particles approach each other. While these results could be useful for modeling of transport of hydrate particles at large length scales, they do not seem to be strongly correlated with the performance of the AAs.

## CONCLUSIONS

Employing classical molecular dynamics simulations, we investigated the interactions between gas hydrate nanoparticles immersed in hydrocarbons in the presence of AAs under industrially relevant conditions, and we correlated the results with the performance of the AAs for hydrate management. The simulated results of hydrate particle cohesive forces for the systems with AAC8, AAC12, and AAC171 in *n*-dodecane and *n*-heptane are quantitatively comparable to those measured from HP-MMF experiments. Excellent agreement between simulated and HP-MMF experimental data suggests that a practical workflow might be possible to predict the performance of AAs. Furthermore, our simulation results reveal, for the first time, that some of the key factors might determine the performance of AAs for the prevention of hydrate agglomeration. These include the orientation of AAs adsorbed at the hydrate−oil interface as well as free energy and entropy changes associated with solvation of AAs, with the latter indicating the degree of AA molecular flexibility upon AA solvation. Our analysis not only explains why the liquid hydrocarbons can affect the AA performance but, once extended to other relevant systems, could also provide a workflow for the accelerated design of new AAs.

## ASSOCIATED CONTENT

### Supporting Information

The Supporting Information is available free of charge at https://pubs.acs.org/doi/10.1021/acsami.1c06309.

Numerical details on fitting simulated force data and results for properties such as density profiles of antiagglomerant molecules between two hydrate particles, locations of minimum and local maxima in the PMF profiles, locations where attraction initiates, and fitting parameters for force−distance curves (PDF)

## AUTHOR INFORMATION


### Corresponding Author

**Alberto Striolo** − *Department of Chemical Engineering, University College London, London WC1E 7JE, U.K.;* orcid.org/0000-0001-6542-8065; Email: a.striolo@ucl.ac.uk

### Authors

**Anh Phan** − *Department of Chemical Engineering, University College London, London WC1E 7JE, U.K.;* orcid.org/0000-0003-2428-6990

**Michail Stamatakis** − *Department of Chemical Engineering, University College London, London WC1E 7JE, U.K.;* orcid.org/0000-0001-8338-8706

**Carolyn A. Koh** − *Center for Hydrate Research, Chemical & Biological Engineering Department, Colorado School of Mines, Golden, Colorado 80401, United States;* orcid.org/0000-0003-3452-4032

Complete contact information is available at: https://pubs.acs.org/10.1021/acsami.1c06309


### Notes

The authors declare no competing financial interest.

## ACKNOWLEDGMENTS

Financial support was generously provided, in part, by the UK EPSRC, under grant number EP/T004282/1, and by the US National Science Foundation, under grant number CBET 2015201 (CAK). Generous allocations of computing time were provided by ARCHER2, the UK National Supercomputing Service (https://www.archer2.ac.uk), and by the University College London Research Computing Platforms Support (Young).

## REFERENCES


(1) Sugahara, T.; Haag, J. C.; Prasad, P. S. R.; Warntjes, A. A.; Sloan, E. D.; Sum, A. K.; Koh, C. A. Increasing Hydrogen Storage Capacity Using Tetrahydrofuran. *J. Am. Chem. Soc.* **2009**, *131*, 14616-+ DOI: 10.1021/ja905819z.

(2) Koh, D. Y.; Kang, H.; Jeon, J.; Ahn, Y. H.; Park, Y.; Kim, H.; Lee, H. Tuning Cage Dimension in Clathrate Hydrates for Hydrogen Multiple Occupancy. *J. Phys. Chem. C* **2014**, *118*, 3324−3330.

(3) Denning, S.; Majid, A. A. A.; Lucero, J. M.; Crawford, J. M.; Carreon, M. A.; Koh, C. A. Metal-Organic Framework HKUST-1 Promotes Methane Hydrate Formation for Improved Gas Storage Capacity. *ACS Appl. Mater. Interfaces* **2020**, *12*, 53510−53518.

(4) Khurana, M.; Veluswamy, H. P.; Daraboina, N.; Linga, P. Thermodynamic and Kinetic Modelling of Mixed $CH_4$-THF Hydrate for Methane Storage Application. *Chem. Eng. J.* **2019**, *370*, 760−771.

(5) Phan, A.; Schlösser, H.; Striolo, A. Molecular Mechanisms by Which Tetrahydrofuran Affects $CO_2$ Hydrate Growth: Implications for Carbon Storage. *Chem. Eng. J.* **2021**, *418*, No. 129423.

(6) Lee, D.; Lee, Y.; Lim, J.; Seo, Y. Guest Enclathration and Structural Transition in $CO_2$ + $N_2$ + Methylcyclopentane Hydrates and Their Significance for $CO_2$ Capture and Sequestration. *Chem. Eng. J.* **2017**, *320*, 43−49.

(7) Moon, S.; Ahn, Y. H.; Kim, H.; Hong, S.; Koh, D. Y.; Park, Y. Secondary Gaseous Guest-Dependent Structures of Binary Neopentyl Alcohol Hydrates and Their Tuning Behavior for Potential Application to $CO_2$ Capture. *Chem. Eng. J.* **2017**, *330*, 890−898.

(8) Babu, P.; Nambiar, A.; He, T. B.; Karimi, I. A.; Lee, J. D.; Englezos, P.; Linga, P. A Review of Clathrate Hydrate Based Desalination to Strengthen Energy-Water Nexus. *ACS Sustainable Chem. Eng.* **2018**, *6*, 8093−8107.

(9) Seo, S. D.; Hong, S. Y.; Sum, A. K.; Lee, K. H.; Lee, J. D.; Lee, B. R. Thermodynamic and Kinetic Analysis of Gas Hydrates for Desalination of Saturated Salinity Water. *Chem. Eng. J.* **2019**, *370*, 980−987.

(10) Kumar, R.; Englezos, P.; Moudrakovski, I.; Ripmeester, J. A. Structure and Composition of $CO_2/H_2$ and $CO_2/H_2/C_3H_8$ Hydrate in Relation to Simultaneous $CO_2$ Capture and $H_2$ Production. *AIChE J.* **2009**, *55*, 1584−1594.

(11) Papadimitriou, N. I.; Tsimpanogiannis, I. N.; Economou, I. G.; Stubos, A. K. Monte Carlo Simulations of the Separation of a Binary Gas Mixture ($CH_4$ + $CO_2$) Using Hydrates. *Phys. Chem. Chem. Phys.* **2018**, *20*, 28026−28038.

(12) Hassanpouryouzband, A.; Joonaki, E.; Farahani, M. V.; Takeya, S.; Ruppel, C.; Yang, J. H.; English, N. J.; Schicks, J. M.; Edlmann, K.; Mehrabian, H.; Aman, Z. M.; Tohidi, B. Gas Hydrates in Sustainable Chemistry. *Chem. Soc. Rev.* **2020**, *49*, 5225−5309.

(13) Fu, X. J.; Jimenez-Martinez, J.; Nguyen, T. P.; Carey, J. W.; Viswanathan, H.; Cueto-Felgueroso, L.; Juanes, R. Crustal Fingering Facilitates Free-Gas Methane Migration through the Hydrate Stability Zone. *Proc. Natl. Acad. Sci. U. S. A.* **2020**, *117*, 31660−31664.

(14) Striolo, A.; Phan, A.; Walsh, M. R. Molecular Properties of Interfaces Relevant for Clathrate Hydrate Agglomeration. *Curr. Opin. Chem. Eng.* **2019**, *25*, 57−66.
(15) Kelland, M. A. *Production Chemicals for the Oil and Gas Industry*, Vol. 72; CRC Press, 2010.
(16) Dendy Sloan, E.; Koh, C. A. *Clathrate Hydrates of Natural Gases*, 3rd ed.; CRC Press − Taylor & Francis Group, 2007; p 752.
(17) Dendy Sloan, E.; Koh, C. A.; Sum, A. *Natural Gas Hydrates in Flow Assurance*; Elsevier: Boston, 2011.
(18) Kinnari, K.; Hundseid, J.; Li, X. Y.; Askvik, K. M. Hydrate Management in Practice. *J. Chem. Eng. Data* **2015**, *60*, 437−446.
(19) Rao, I.; Koh, C. A.; Sloan, E. D.; Sum, A. K. Gas Hydrate Deposition on a Cold Surface in Water-Saturated Gas Systems. *Ind. Eng. Chem. Res.* **2013**, *52*, 6262−6269.
(20) Dapena, J. A.; Majid, A. A.; Srivastava, V.; Wang, Y.; Charlton, T. B.; Gardner, A. A.; Sloan, E. D.; Zerpa, L. E.; Wu, D. T.; Koh, C. A. Gas Hydrate Management Strategies Using Anti-Agglomerants: Continuous & Transient Large-Scale Flowloop Studies. In *Offshore Technology Conference*; Offshore Technology Conference: Houston, Texas, USA, 2017; p 16.
(21) Kelland, M. A. History of the Development of Low Dosage Hydrate Inhibitors. *Energy Fuels* **2006**, *20*, 825−847.
(22) Perrin, A.; Musa, O. M.; Steed, J. W. The Chemistry of Low Dosage Clathrate Hydrate Inhibitors. *Chem. Soc. Rev.* **2013**, *42*, 1996−2015.
(23) Aman, Z. M.; Olcott, K.; Pfeiffer, K.; Sloan, E. D.; Sum, A. K.; Koh, C. A. Surfactant Adsorption and Interfacial Tension Investigations on Cyclopentane Hydrate. *Langmuir* **2013**, *29*, 2676−2682.
(24) Li, S. X.; Lv, R. J.; Yan, Z. S.; Huang, F.; Zhang, X. R.; Chen, G. J.; Yue, T. T. Design of Alanine-Rich Short Peptides as a Green Alternative of Gas Hydrate Inhibitors: Dual Methyl Group Docking for Efficient Adsorption on the Surface of Gas Hydrates. *ACS Sustainable Chem. Eng.* **2020**, *8*, 4256−4266.
(25) Jimenez-Angeles, F.; Firoozabadi, A. Hydrophobic Hydration and the Effect of Nacl Salt in the Adsorption of Hydrocarbons and Surfactants on Clathrate Hydrates. *ACS Cent. Sci.* **2018**, *4*, 820−831.
(26) Mehrabian, H.; Walsh, M. R.; Trout, B. L. In Silico Analysis of the Effect of Alkyl Tail Length on Antiagglomerant Adsorption to Natural Gas Hydrates in Brine. *J. Phys. Chem. C* **2019**, *123*, 17239−17248.
(27) Mehrabian, H.; Trout, B. L. In Silico Engineering of Hydrate Anti-Agglomerant Molecules Using Bias-Exchange Metadynamics Simulations. *J. Phys. Chem. C* **2020**, *124*, 18983−18992.
(28) Brown, E. P.; Koh, C. A. Competitive Interfacial Effects of Surfactant Chemicals on Clathrate Hydrate Particle Cohesion. *Energy Fuels* **2016**, *30*, 8065−8071.
(29) Chua, P. C.; Kelland, M. A. Study of the Gas Hydrate Antiagglomerant Performance of a Series of Mono- and Bis-Amine Oxides: Dual Antiagglomerant and Kinetic Hydrate Inhibition Behavior. *Energy Fuels* **2018**, *32*, 1674−1684.
(30) Bellucci, M. A.; Walsh, M. R.; Trout, B. L. Molecular Dynamics Analysis of Anti-Agglomerant Surface Adsorption in Natural Gas Hydrates. *J. Phys. Chem. C* **2018**, *122*, 2673−2683.
(31) Bui, T.; Phan, A.; Monteiro, D.; Lan, Q.; Ceglio, M.; Acosta, E.; Krishnamurthy, P.; Striolo, A. Evidence of Structure-Performance Relation for Surfactants Used as Antiagglomerants for Hydrate Management. *Langmuir* **2017**, *33*, 2263−2274.
(32) Phan, A.; Bui, T.; Acosta, E.; Krishnamurthy, P.; Striolo, A. Molecular Mechanisms Responsible for Hydrate Anti-Agglomerant Performance. *Phys. Chem. Chem. Phys.* **2016**, *18*, 24859−24871.
(33) Bui, T.; Sicard, F.; Monteiro, D.; Lan, Q.; Ceglio, M.; Burress, C.; Striolo, A. Antiagglomerants Affect Gas Hydrate Growth. *J. Phys. Chem. Lett.* **2018**, *9*, 3491−3496.
(34) Chua, P. C.; Kelland, M. A. Study of the Gas Hydrate Anti-Agglomerant Performance of a Series of N-Alkyl-Tri(N-Butyl)-Ammonium Bromides. *Energy Fuels* **2013**, *27*, 1285−1292.
(35) Wang, W. C.; Li, Y. X.; Liu, H. H.; Zhao, P. F. Study of Agglomeration Characteristics of Hydrate Particles in Oil/Gas Pipelines. *Adv. Mech. Eng.* **2015**, *7*, No. 457050.
(36) Israelachvili, J. N. *Intermolecular and Surface Forces*, 2nd ed.; Academic Press, 1991.
(37) Aman, Z. M.; Joshi, S. E.; Sloan, E. D.; Sum, A. K.; Koh, C. A. Micromechanical Cohesion Force Measurements to Determine Cyclopentane Hydrate Interfacial Properties. *J. Colloid Interface Sci.* **2012**, *376*, 283−288.
(38) Brown, E. P.; Hu, S. J.; Wells, J.; Wang, X. H.; Koh, C. A. Direct Measurements of Contact Angles on Cyclopentane Hydrates. *Energy Fuels* **2018**, *32*, 6619−6626.
(39) Dieker, L. E.; Aman, Z. M.; George, N. C.; Sum, A. K.; Sloan, E. D.; Koh, C. A. Micromechanical Adhesion Force Measurements between Hydrate Particles in Hydrocarbon Oils and Their Modifications. *Energy Fuels* **2009**, *23*, 5966−5971.
(40) Aman, Z. M.; Dieker, L. E.; Aspenes, G.; Sum, A. K.; Sloan, E. D.; Koh, C. A. Influence of Model Oil with Surfactants and Amphiphilic Polymers on Cyclopentane Hydrate Adhesion Forces. *Energy Fuels* **2010**, *24*, 5441−5445.
(41) Yang, S. O.; Kleehammer, D. M.; Huo, Z. X.; Sloan, E. D.; Miller, K. T. Temperature Dependence of Particle-Particle Adherence Forces in Ice and Clathrate Hydrates. *J. Colloid Interface Sci.* **2004**, *277*, 335−341.
(42) Aman, Z. M.; Brown, E. P.; Sloan, E. D.; Sum, A. K.; Koh, C. A. Interfacial Mechanisms Governing Cyclopentane Clathrate Hydrate Adhesion/Cohesion. *Phys. Chem. Chem. Phys.* **2011**, *13*, 19796−19806.
(43) Aspenes, G.; Dieker, L. E.; Aman, Z. M.; Hoiland, S.; Sum, A. K.; Koh, C. A.; Sloan, E. D. Adhesion Force between Cyclopentane Hydrates and Solid Surface Materials. *J. Colloid Interface Sci.* **2010**, *343*, 529−536.
(44) Lee, B. R.; Sum, A. K. Micromechanical Cohesion Force between Gas Hydrate Particles Measured under High Pressure and Low Temperature Conditions. *Langmuir* **2015**, *31*, 3884−3888.
(45) Wang, S. L.; Hu, S. J.; Brown, E. P.; Nakatsuka, M. A.; Zhao, J. F.; Yang, M. J.; Song, Y. C.; Koh, C. A. High Pressure Micromechanical Force Measurements of the Effects of Surface Corrosion and Salinity on $CH_4/C_2H_6$ Hydrate Particle-Surface Interactions. *Phys. Chem. Chem. Phys.* **2017**, *19*, 13307−13315.
(46) Hu, S. J.; Koh, C. A. Interfacial Properties and Mechanisms Dominating Gas Hydrate Cohesion and Adhesion in Liquid and Vapor Hydrocarbon Phases. *Langmuir* **2017**, *33*, 11299−11309.
(47) Hu, S. J.; Koh, C. A. $CH_4/C_2H_6$ Gas Hydrate Interparticle Interactions in the Presence of Anti-Agglomerants and Salinity. *Fuel* **2020**, *269*, No. 117208.
(48) Hu, S.; Vo, L.; Monteiro, D.; Bodnar, S.; Prince, P.; Koh, C. A. Structural Effects of Gas Hydrate Antiagglomerant Molecules On interfacial Interparticle Force Interactions. *Langmuir* **2021**, *37*, 1651−1661.
(49) Bui, T.; Monteiro, D.; Vo, L.; Striolo, A. Synergistic and Antagonistic Effects of Aromatics on the Agglomeration of Gas Hydrates. *Sci. Rep.* **2020**, *10*, No. 5496.
(50) Sicard, F.; Bui, T.; Monteiro, D.; Lan, Q.; Ceglio, M.; Burress, C.; Striolo, A. Emergent Properties of Antiagglomerant Films Control Methane Transport: Implications for Hydrate Management. *Langmuir* **2018**, *34*, 9701−9710.
(51) Takeuchi, F.; Hiratsuka, M.; Ohmura, R.; Alavi, S.; Sum, A. K.; Yasuoka, K. Water Proton Configurations in Structures I, II, and H Clathrate Hydrate Unit Cells. *J. Chem. Phys.* **2013**, *138*, No. 124504.
(52) Abascal, J. L. F.; Sanz, E.; Fernandez, R. G.; Vega, C. A Potential Model for the Study of Ices and Amorphous Water: TIP4P/Ice. *J. Chem. Phys.* **2005**, *122*, No. 234511.
(53) Walsh, M. R.; Koh, C. A.; Sloan, E. D.; Sum, A. K.; Wu, D. T. Microsecond Simulations of Spontaneous Methane Hydrate Nucleation and Growth. *Science* **2009**, *326*, 1095−1098.
(54) Wang, J. M.; Wolf, R. M.; Caldwell, J. W.; Kollman, P. A.; Case, D. A. Development and Testing of a General Amber Force Field. *J. Comput. Chem.* **2004**, *25*, 1157−1174.
(55) Case, D. A.; Babin, V.; Berryman, J. T.; Betz, R. M.; Cai, Q.; Cerutti, D. S.; Cheatham, T. E. I.; Darden, T. A.; Duke, R. E.; Gohlke, H.; Goetzm, A. W.; Gusarov, S.; Homeyer, N.; Janowski, P.; Kaus, J.;


https://doi.org/10.1021/acsami.1c06309
ACS Appl. Mater. Interfaces 2021, 13, 40002−40012

Kolossváry, I.; Kovalenko, A.; Lee, T. S.; LeGrand, S.; Luchko, T. L. R.; Madej, B.; Merz, K. M.; Paesani, F.; Roe, D. R.; Roitberg, A.; Sagui, C.; Salomon-Ferrer, R.; Seabra, G.; Simmerling, C. L.; Smith, W.; Swails, J.; Walker, R. C.; Wang, J.; Wolf, R. M.; Wu, X.; Kollman, P. A. *Amber 14*; University of California: San Francisco, 2014.

(56) Martin, M. G.; Siepmann, J. I. Transferable Potentials for Phase Equilibria. 1. United-Atom Description of N-Alkanes. *J. Phys. Chem. B* **1998**, *102*, 2569−2577.

(57) Smith, D. E.; Dang, L. X. Computer-Simulations of Nacl Association in Polarizable Water. *J. Chem. Phys.* **1994**, *100*, 3757−3766.

(58) Mamatkulov, S.; Fyta, M.; Netz, R. R. Force Fields for Divalent Cations Based on Single-Ion and Ion-Pair Properties. *J. Chem. Phys.* **2013**, *138*, No. 024505.

(59) Hartkamp, R.; Coasne, B. Structure and Transport of Aqueous Electrolytes: From Simple Halides to Radionuclide Ions. *J. Chem. Phys.* **2014**, *141*, No. 124508.

(60) Eastwood, J. W.; Hockney, R. W.; Lawrence, D. N. P3M3DP—the 3-Dimensional Periodic Particle-Particle-Particle-Mesh Program. *Comput. Phys. Commun.* **1980**, *19*, 215−261.

(61) Allen, M. P.; Tildesley, D. J. *Computer Simulation of Liquids*; Oxford University Press: Oxford, U.K., 2004.

(62) Abraham, M. J.; Murtola, T.; Schulz, R.; Páll, S.; Smith, J. C.; Hess, B.; Lindahl, E. Gromacs: High Performance Molecular Simulations through Multi-Level Parallelism from Laptops to Supercomputers. *SoftwareX* **2015**, *1*, 19−25.

(63) Hub, J. S.; De Groot, B. L.; Van Der Spoel, D. G_Wham-a Free Weighted Histogram Analysis Implementation Including Robust Error and Autocorrelation Estimates. *J. Chem. Theory Comput.* **2010**, *6*, 3713−3720.

(64) Griffiths, M. Z.; Shinoda, W. Analyzing the Role of Surfactants in the Colloidal Stability of Nanoparticles in Oil through Coarse-Grained Molecular Dynamics Simulations. *J. Phys. Chem. B* **2021**, *125*, 6315−6321.

(65) Vo, M. D.; Papavassiliou, D. V. Interaction between Polymer-Coated Carbon Nanotubes with Coarse-Grained Computations. *Chem. Phys. Lett.* **2017**, *685*, 77−83.

(66) Motulsky, H. J.; Brown, R. E. Detecting Outliers When Fitting Data with Nonlinear Regression—a New Method Based on Robust Nonlinear Regression and the False Discovery Rate. *BMC Bioinf.* **2006**, *7*, 123.

(67) McCulfor, J.; Himes, P.; Anklam, M. R. The Effects of Capillary Forces on the Flow Properties of Glass Particle Suspensions in Mineral Oil. *AIChE J.* **2011**, *57*, 2334−2340.

(68) Anklam, M. R.; York, J. D.; Helmerich, L.; Firoozabadi, A. Effects of Antiagglomerants on the Interactions between Hydrate Particles. *AIChE J.* **2008**, *54*, 565−574.

(69) Rabinovich, Y. I.; Esayanur, M. S.; Moudgil, B. M. Capillary Forces between Two Spheres with a Fixed Volume Liquid Bridge: Theory and Experiment. *Langmuir* **2005**, *21*, 10992−10997.

(70) Kaimaki, D. M.; Smith, B. E.; Durkan, C. On the Use of Nanomechanical Atomic Force Microscopy to Characterise Oil-Exposed Surfaces. *RSC Adv.* **2018**, *8*, 6680−6689.

(71) Sicard, F.; Striolo, A. Role of Structural Rigidity and Collective Behaviour in the Molecular Design of Gas Hydrates Anti-Agglomerants. 2021 rXiv preprint *arXiv:2012.09765*.

(72) Nayar, D.; Yadav, H. O. S.; Jabes, B. S.; Chakravarty, C. Relating Structure, Entropy, and Energy of Solvation of Nanoscale Solutes: Application to Gold Nanoparticle Dispersions. *J. Phys. Chem. B* **2012**, *116*, 13124−13132.

(73) Srivastava, A.; Debnath, A. Asymmetry and Rippling in Mixed Surfactant Bilayers from All-Atom and Coarse-Grained Simulations: Interdigitation and Per Chain Entropy. *J. Phys. Chem. B* **2020**, *124*, 6420−6436.

(74) Schlitter, J. Estimation of Absolute and Relative Entropies of Macromolecules Using the Covariance-Matrix. *Chem. Phys. Lett.* **1993**, *215*, 617−621.

(75) Schafer, H.; Mark, A. E.; Van Gunsteren, W. F. Absolute Entropies from Molecular Dynamics Simulation Trajectories. *J. Chem. Phys.* **2000**, *113*, 7809−7817.

(76) Andricioaei, I.; Karplus, M. On the Calculation of Entropy from Covariance Matrices of the Atomic Fluctuations. *J. Chem. Phys.* **2001**, *115*, 6289−6292.

(77) Wilson, N. T.; Johnston, R. L. Modelling Gold Clusters with an Empirical Many-Body Potential. *Eur. Phys. J. D* **2000**, *12*, 161−169.

(78) Hikiri, S.; Yoshidome, T.; Ikeguchi, M. Computational Methods for Configurational Entropy Using Internal and Cartesian Coordinates. *J. Chem. Theory Comput.* **2016**, *12*, 5990−6000.

(79) Baron, R.; De Vries, A. H.; Hunenberger, P. H.; Van Gunsteren, W. F. Comparison of Atomic-Level and Coarse-Grained Models for Liquid Hydrocarbons from Molecular Dynamics Configurational Entropy Estimates. *J. Phys. Chem. B* **2006**, *110*, 8464−8473.

(80) Orozco, M.; Luque, F. J. Theoretical Methods for the Description of the Solvent Effect in Biomolecular Systems. *Chem. Rev.* **2000**, *100*, 4187−4225.

(81) Lynden-Bell, R. M.; Giovambattista, N.; Debenedetti, P. G.; Head-Gordon, T.; Rossky, P. J. Hydrogen Bond Strength and Network Structure Effects on Hydration of Non-Polar Molecules. *Phys. Chem. Chem. Phys.* **2011**, *13*, 2748−2757.

(82) Arnold, T.; Thomas, R. K.; Castro, M. A.; Clarke, S. M.; Messe, L.; Inaba, A. The Crystalline Structures of the Even Alkanes Hexane, Octane, Decane, Dodecane and Tetradecane Monolayers Adsorbed on Graphite at Submonolayer Coverages and from the Liquid. *Phys. Chem. Chem. Phys.* **2002**, *4*, 345−351.

(83) Naullage, P. M.; Bertolazzo, A. A.; Molinero, V. How Do Surfactants Control the Agglomeration of Clathrate Hydrates? *ACS Cent. Sci.* **2019**, *5*, 428−439.

(84) Nagai, T.; Tsurumaki, S.; Urano, R.; Fujimoto, K.; Shinoda, W.; Okazaki, S. Position-Dependent Diffusion Constant of Molecules in Heterogeneous Systems as Evaluated by the Local Mean Squared Displacement. *J. Chem. Theory Comput.* **2020**, *16*, 7239−7254.

(85) Berne, B. J.; Borkovec, M.; Straub, J. E. Classical and Modern Methods in Reaction-Rate Theory. *J. Phys. Chem.* **1988**, *92*, 3711−3725.

(86) Hummer, G. Position-Dependent Diffusion Coefficients and Free Energies from Bayesian Analysis of Equilibrium and Replica Molecular Dynamics Simulations. *New J. Phys.* **2005**, *7*, 34.

(87) Gaalswyk, K.; Awoonor-Williams, E.; Rowley, C. N. Generalized Langevin Methods for Calculating Transmembrane Diffusivity. *J. Chem. Theory Comput.* **2016**, *12*, 5609−5619.



https://doi.org/10.1021/acsami.1c06309
*ACS Appl. Mater. Interfaces* 2021, 13, 40002−40012